TU Delft

Delft University of Technology

Experimental evaluation of a morphing leading edge concept

Sodja, Jurij; Martinez, Marcias J.; Simpson, John C.; De Breuker, Roeland

DOI
10.1177/1045389X19862369

Publication date
2019

Published in
Journal of Intelligent Material Systems and Structures

Citation (APA)
Sodja, J., Martinez, M. J., Simpson, J. C., & De Breuker, R. (2019). Experimental evaluation of a morphing leading edge concept. *Journal of Intelligent Material Systems and Structures*, *30*(18-19), 2953-2969. https://doi.org/10.1177/1045389X19862369

Important note
To cite this publication, please use the final published version (if applicable).
Please check the document version above.

Copyright
Other than for strictly personal use, it is not permitted to download, forward or distribute the text or part of it, without the consent of the author(s) and/or copyright holder(s), unless the work is under an open content license such as Creative Commons.

Takedown policy
Please contact us and provide details if you believe this document breaches copyrights.
We will remove access to the work immediately and investigate your claim.

This work is downloaded from Delft University of Technology.
For technical reasons the number of authors shown on this cover page is limited to a maximum of 10.

Check for updates

Journal of Intelligent Material Systems and Structures

Original Article

Journal of Intelligent Material Systems and Structures
1–17
© The Author(s) 2019
DOI: 10.1177/1045389X19862369
journals.sagepub.com/home/jim
SAGE

Experimental evaluation of a morphing leading edge concept

Jurij Sodja[1], Marcias J Martinez[2], John C Simpson[3] and Roeland De Breuker[1]

Abstract

This article presents an experimental evaluation of a morphing leading edge demonstrator by investigating its morphed shape, the level of induced strains in the airfoil skin, the actuation force, and the morphing mechanism's capability to lock and transfer the applied loads. In addition, a finite element model of the demonstrator is assembled comprising an elastic morphing skin and a kinematic morphing mechanism. The obtained results are used to assess whether the demonstrator performs according to the design objectives, such as the target shape, the character of the morphing deformation and the morphing mechanism locking, applied during the design process. The comparison between experimental and numerical results yielded a good agreement in terms of observed morphed shape and pertaining strains. The average difference in morphed shape was less than 0.08% chord at the maximum actuator extension. The observed difference in the respective strains was less than 400 micro-strains. A significant difference, up to 70%, was observed in the actuation force, which was attributed to the modelling assumptions and to the force measurement technique employed in the experiment. Nevertheless, both results show good qualitative agreement showing similar trends.

Keywords

Morphing, droop nose, leading edge, experiment

1. Introduction

Despite tremendous technological headway in commercial aviation over the past 60 years, the increase in the amount of air traffic requires further reductions in engine and noise emissions to render commercial aviation sustainable in the long-term perspective. In response, Advisory Council for Aeronautics Research in Europe (ACARE) put forth a set of ambitious goals: a 50% reduction in carbon dioxide, an 80% reduction in nitrogen oxides and a 50% reduction in perceived noise relative to the emission and noise levels reported in the year 2000 (ACARE, 2010). A similar initiative was also started in the United States by NASA's Environmentally Responsible Aviation (ERA) project. As a result, many research projects investigating, among others, novel airframe configurations, propulsion and laminar flow technologies were funded by both the EU and the United States (Graham et al., 2014; Suder, 2012). According to Barbarino et al. (2011) and Weisshaar (2013), airfoil morphing can contribute to aircraft performance in several ways. It can improve laminar and basic turbulent flow conditions. It can be utilised for continuous lift-to-drag ratio optimisation or adaptation to specific flight phase requirements such as take-off, cruise and landing. It can also provide for more efficient flight control mechanisms. Hence, it is no surprise that morphing wings, airfoils and high-lift devices were the focus of research in several research projects, such as, among others, SADE, SARISTU and NOVEMOR (Kintscher et al., 2011, 2014; Vasista et al., 2016).

In particular, morphing high-lift devices such as the morphing leading edge investigated in this article bear great potential for improving the aerodynamic efficiency of future aircraft as well as reducing their acoustic intensity by allowing for flow laminarisation (Morgan, 1986) and by eliminating major noise sources associated with conventional high-lift devices (Casalino

[1]Aerospace Structures & Computational Mechanics, Faculty of Aerospace Engineering, Delft University of Technology, Delft, The Netherlands
[2]Clarkson University, Potsdam, NY, USA
[3]Fraunhofer-Institut für Bauphysik, Stuttgart, Germany

Corresponding author:
Jurij Sodja, Aerospace Structures & Computational Mechanics, Faculty of Aerospace Engineering, Delft University of Technology, Kluyverweg 1, 2629 HS Delft, The Netherlands.
Email: j.sodja@tudelft.nl

et al., 2008; Dobrzynski et al., 2001). These technologies could, therefore, prove essential in achieving ambitious environmental goals posed by ACARE and NASA.

A lot of research effort has already been invested into various aspects concerning morphing droop nose. As reported by Monner et al. (2009), the 'active rib' concept initially proposed by Dornier (Patent DE2907912-A1, Dornier company, 1979) was investigated and further developed within the SADE project. A dedicated integrated workflow was established to first optimise the droop nose shape in combination with the flap settings, derive the morphing skin properties and finally develop the kinematic mechanism. Kintscher et al. (2011) used the developed workflow to design a demonstrator for the wind tunnel test envisioned within the project. The demonstrator was ground tested, and Monner et al. (2012) reported good overall agreement with the numerical model concerning morphing accuracy. Kirn and Storm (2014) further improved the 'active rib' concept by reducing its mass and kinematic complexity within the SARISTU project.

Opposed to conventional morphing mechanisms investigated in SADE, two morphing droop nose concepts based on compliant mechanism were investigated in the NOVEMOR project (Vasista et al., 2016). The first concept was developed by DLR following a similar workflow previously used in the development of the 'active rib' concept (Vasista et al., 2015). First, the morphing skin was designed to optimally match the required target shape, followed by the topology optimisation of the pertinent compliant mechanism and the actuator support. A demonstrator was built and tested on a test bench focusing on the performance of the compliant mechanism in combination with different morphing skins of various thicknesses. However, other loads, such as consolidated aerodynamic loads, were not applied during the test. The second concept was developed by De Gaspari and Ricci (2011, 2014) using a two-level approach with a significant difference being that in the first level the droop nose shape is optimised for maximum C_L and minimum strain energy rather than trying to match a predefined morphed shape. An internal compliant mechanism yielding the obtained optimised droop nose shape is then synthesised using a topology optimisation coupled to a genetic algorithm in the second step. The developed approach was later used for designing and manufacturing of a scaled morphing demonstrator which was tested in the wind tunnel. De Gaspari et al. (2016) showed good agreement between the experimentally obtained and numerically predicted morphed shape of the droop nose as well as aerodynamic benefits of using a morphing droop nose, especially in combination with the morphing trailing edge. One of the reported benefits was significantly delayed stall.

Just recently Rudenko et al. (2018) presented an extremely deformable leading edge concept. The design of the inner morphing mechanism of the concept is based on the methodology developed by DLR within the SADE project. Nevertheless, the main novelty of the concept is the introduction of the 'curvature morphing skin' which is characterised by highly anisotropic behaviour therewith allowing the concept to achieve a high degree of droop. A section of the full-scale leading edge was built and tested on the test bench. Moderate agreement between finite element simulations and experiment was observed. Sensitivity to manufacturing inaccuracies along with simplified numerical modelling of skin-stringer connections was identified as the primary origin of discrepancies.

The morphing leading edge demonstrator presented here was developed during the Leading Edge Topology Optimised Design and Demonstrator (LeaTop) project as part of the EU CleanSky Green Regional Aircraft (GRA) initiative. Similar to previously presented projects, one of the objectives was to develop, manufacture and test a functional morphing leading edge demonstrator that can effectively transition from its original configuration, the cruise shape, to its target configuration, the high-lift shape, while subjected to full aerodynamic loads. In addition, an important objective of the project was to address also more practical considerations which limit the integration of such morphing devices in commercial aviation at a larger scale and demonstrate a feasible solution. Such considerations are whether an accurate cruise shape can be maintained during flight; how to transfer aerodynamic loads from the morphing skin of the leading edge into the wing primary structure without causing excessive stress concentrations at the skin-spar connection; and whether conventional materials, such as aluminium, can be used for the morphing skin, therewith mitigating bird-strike and de-icing issues commonly associated with composite structures.

The demonstrator was designed by Mauchle et al. (2012) using an integrated aeroelastic-morphing framework developed by Thuwis et al. (2010, 2011) at Delft University of Technology. The framework allows for concurrent optimisation of the morphing skin properties and the morphing mechanism in order to meet the required target shape as accurately as possible while, at the same time, also minimising strains in the morphing skin and corresponding reaction and actuation forces in the morphing mechanism. The design is performed in two steps. First, topology optimisation is used to optimise the skin properties and obtain the initial mechanism layout. In the second step, a detailed design is performed to account for practicalities such as mechanism connection to the skin and pertinent offsets due to the finite dimension of mechanical components in the load introduction points.

This work presents the experimental evaluation of the morphing leading edge concept with respect to the

considerations addressed in the LeaTop project. The experiments were therefore divided into three parts: strain evaluation in the airfoil skin, morphing mechanism locking and load transfer capability, and shape measurements of the morphed skin. In addition, a finite element model (FEM) of the demonstrator was developed to compare with the experimental results and to obtain better insight into the behaviour of the demonstrator.

The article is structured as follows. First, the experimental setup and the employed measurement techniques are presented. Next, the FEM is presented followed by the discussion of the obtained results. Finally, all the findings and conclusions are summed up in the 'Conclusion' section.

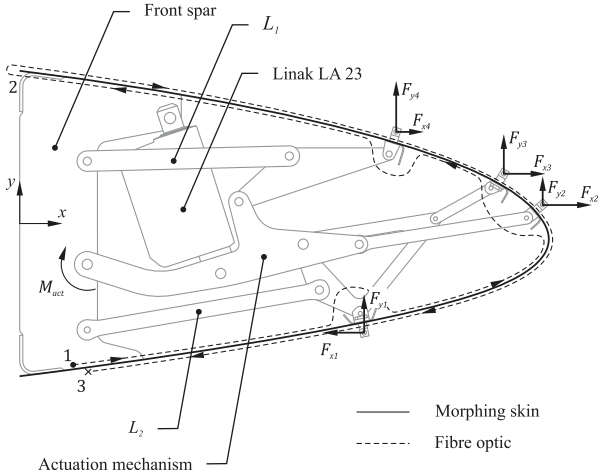

Figure 1. LeaTop morphing leading edge demonstrator.

2. Experimental setup

The experimental work was divided into three parts: evaluation of strain in the airfoil skin, locking capabilities of the morphing mechanism and shape measurements of the morphed skin. Each part is designed to test the demonstrator for important requirements that were imposed during the conceptual design process. Strain measurements validate the requirement that the airfoil skin undergoes primarily bending deformation during the morphing process to keep the induced strain as low as possible. Evaluation of the locking capability of the morphing mechanism validates the ability of the demonstrator to preserve the shape of the airfoil under aerodynamic loads at cruise conditions. Within this scope, the ability of the morphing mechanism to transfer the applied loads efficiently from the airfoil skin into the main spar is also tested. Finally, shape measurements are used to assess to what extent the morphing mechanism can match the target shape which was prescribed during the design of the demonstrator.

Table 1. Overview of the experimental setup.

Parameter	Unit	Quantity
Demonstrator dimensions		
Section location	m	3.229
Section chord	m	3.460
Length, width, height	m^3	0.519, 0.200, 0.300
Skin thickness	mm	1.2
Morphing skin material		
Material	–	Aluminium 7075T6
Young's modulus, E_{alu}	GPa	70
Shear modulus, G_{alu}	GPa	27
Poisson's ratio, ν_{alu}	–	0.33
Yield stress, $\sigma_{y,\,alu}$	GPa	0.48
Actuator properties		
Type	–	Linak LA 23
Blocked force	N	2500
Stroke	mm	49

2.1. Morphing leading edge demonstrator

The morphing leading edge demonstrator was designed as a section of high-lift system of the Clean Sky GRA Integrated Technology Demonstrator (ITD) (Mauchle et al., 2012). The selected section was positioned 3.229 m from the fuselage centerline which is 1/3 along the primary high-lift system on the wing. The sectional chord length was 3.46 m. The front spar was positioned at 15% chord, which also limited the extent of the droop nose to a length of 0.519 m and a height at the front spar of 0.3 m. The width of the demonstrator was 0.2 m. The demonstrator width was chosen based on the practical considerations such as cost of manufacturing and ease of handling in the laboratory. However, the optimum pitch of the morphing sections in the GRA wing remains to be determined in a future design study which is beyond the scope of this article. Finally, the demonstrator had to achieve a minimum of 5 deg droop. The morphing skin and the mechanism were manufactured out of aluminium 7000 series with Young's modulus, $E_{alu} = 71$ GPa, shear modulus, $G_{alu} = 27$ GPa, and Poisson's ratio, $\nu_{alu} = 0.33$. The skin thickness was constant at 1.2 mm. The final design of the demonstrator including the internal mechanism is shown in Figure 1 and the main characteristics are listed in Table 1.

A Linak LA 23 series linear actuator was used for actuation of the demonstrator. The selected actuator is capable of developing 2500 N of actuation force and has a rated maximum stroke of 49 mm. The actuator is equipped with a hall potentiometer sensor in order to monitor its extension and a simple on/off electronic control switch to extend or contract its pushrod (Linak, 2012). Furthermore, by monitoring the electric current consumption of the actuator, the actuation force could be estimated. Therefore, a LabView virtual instrument was developed to drive and monitor the electric

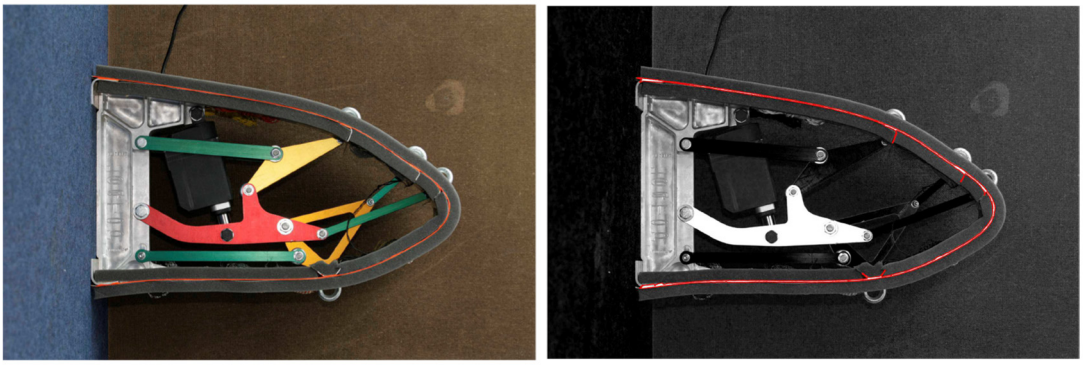

(a) (b)

Figure 2. Edge detection of the morphing demonstrator: (a) original picture and (b) processed picture.

actuation signal provided to the actuator. This way, data about the actuation behaviour, namely actuator's extension, actuating speed and required actuation force, were obtained.

2.2. Strain measurements

The airfoil skin was instrumented with a strain measurement system. A Rayleigh backscattering fibre optic distributed sensing system (ODISI B from LUNA Technologies; Luna Innovations Inc. 2012) was employed in order to acquire as much information as possible on the strain distribution along the perimeter of the leading edge skin (Güemes et al., 2010). The integration of the fibre optic strain sensor is depicted in Figure 1.

A fibre optic sensor was attached to the airfoil skin using epoxy resin. The Rayleigh Backscattering system allows for a strain measurement every 1.25 mm along the length of the optical fibre up to a total length of 10 m with a maximum data acquisition rate of 23.8 Hz. Thus, it was decided to glue the fibre along the entire perimeter of the leading edge both on the inner and outer surface of the skin. Placement of the sensing fibre along the entire perimeter of the leading edge enabled a detailed analysis of bending and tensional deformation of the airfoil skin during morphing. On the other hand, placing the fibre symmetrically on both sides of the demonstrator allowed for detection of potential misalignment or asymmetry in the morphed demonstrator. A schematic path of the sensing fibre is depicted in Figure 1. The fibre started at location 1 and then followed the inner contour of the skin up to location 2 where it was guided to the outer side of the skin. At the stiffener locations, the fibre had to be detached from the skin, guided over the stiffener and then re-attached to the skin. The measurements over these segments of the fibre were discarded since they did not correspond to the actual strain in the skin. The fibre placed on the outside of the skin then followed the contour of the skin up to location 3 where it was guided to the far edge of the skin and then placed in the reversed order.

2.3. Shape measurements

The deformed shape of the airfoil skin was measured using photogrammetry. A digital camera was used to photograph the morphing demonstrator from a fixed position. It was ensured that the camera was far enough from the demonstrator such that the perspective distortions were negligible and that the same scaling factor could be used all around the perimeter of the skin. In order to enhance the visibility of the edge of the skin, the edge was painted in orange and masked with grey foam as can be observed in Figure 2(a). The captured images were then converted to black and white images. Since the skin edge was coloured orange, it was decided to substitute the red tones with the white colour during the conversion of the images. This way a good contrast was achieved between the orange skin edge and the grey masking foam. An image recognition algorithm, developed in MATLAB, was then used in order to process the contour of the black and white images and thus extract the contours of the morphed skin. An example of a processed image is shown in Figure 2(b) where the result of the edge recognition process is plotted by a red line. One can observe that the skin edge along with the stringers was correctly identified along the entire perimeter of the edge.

2.4. Morphing mechanism locking

Morphing mechanism features several 4 bar submechanisms which were realised by adding links L_1 and L_2, as shown in Figure 1, in the second step of the design process (Mauchle et al., 2012).

It was important to demonstrate that the morphing mechanism was capable of transferring the applied loads to the main spar effectively. Due to its design, the mechanism is effectively locked in position if the

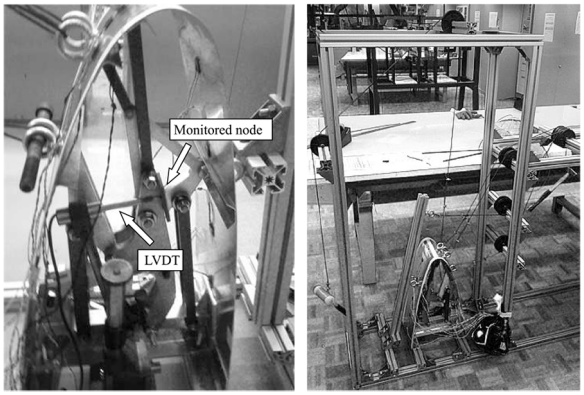

Figure 3. Setup for testing of mechanism locking: (a) mechanism displacement measurement using an LVDT and (b) test rig for application of condensed aerodynamic loads.

Table 2. Maximum discrete applied loads.

i	F_{xi} (N)	F_{yi} (N)	x_i (m)	y_i (m)
1	−51.6	268.4	0.340	−0.097
2	694.3	76.8	0.509	0.009
3	297.5	492.7	0.472	0.039
4	260.2	1,043.7	0.369	0.080

actuator is not moving, which makes the mechanism a statically determinate system. Therefore, it is sufficient to measure a displacement of one node in the mechanism in order to assess how the mechanism copes with the applied load. A small or negligible displacement of the measured node under applied load indicates that the mechanism is effectively locked. The displacement of the selected member was measured using a linear voltage displacement transducer (LVDT). The position of the LVDT and the monitored mechanism member is shown in Figure 3(a). Representative distributed aerodynamic forces were reduced to a set of four discrete load vectors (F_{xi}, F_{yi}); $i = 1, 2, 3, 4$ which introduction points are shown in Figure 1. The maximum applied loads are summarised in Table 2. They correspond to the aerodynamic forces exerted on a 1 m wide section of the leading edge in cruise conditions. The maximum cumulative load applied in the experiment is compared to the corresponding cumulative aerodynamic load in Table 3. The comparison shows that the cumulative forces are well recovered; however, the actuation moment, M_{act}, is not. This was not a concern since the M_{act} applied during the experiment exceeded the aerodynamic moment meaning that the experiment was performed in a conservative manner. To apply the loads, a special test rig comprising a system of pulleys and weights was built as shown in Figure 3(b).

Table 3. Total maximum applied load in comparison to aerodynamic load.

Loads	Aerodynamic	Applied	Unit
$\sum F_{xi}$	1200.4	1200.4	N
$\sum F_{yi}$	1881.5	1881.5	N
$\sum M_{act}$	374.0	664.8	Nm

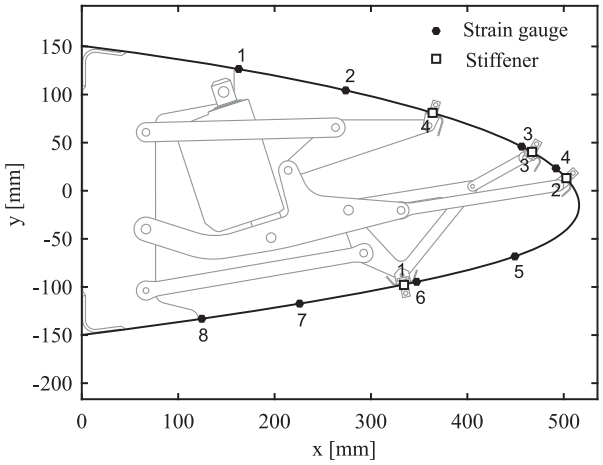

Figure 4. Strain gauge locations and load introduction points.

In addition to the displacement of the mechanism, the deformation of the airfoil skin in terms of induced strains was also measured at a number of critical locations using strain gauges. In this case, strain gauges were used instead of the optical fibre since it was easier to place them close to the stiffeners. The selected locations were close to the load introduction points, at the top and bottom skin-spar connection and at the tip of the leading edge where the maximum strain was expected according to the finite element analysis. The exact location of the placed strain gauges is also shown in Figure 4. Strain gauges were placed in pairs on both the inner and outer surface of the skin to be able to differentiate between axial and bending strains.

3. Finite Element Model

For the sake of comparison, the morphing leading edge was modelled in a commercial finite element (FE) analysis tool ANSYS Mechanical®, Academic Research, Release 15.0. The geometry of the FEM was defined using the 3D CATIA® model previously used for the manufacturing of the morphing leading edge demonstrator. To ensure that the CATIA® model and the actual demonstrator were indeed similar in dimensions, the actuation mechanism of the demonstrator was measured and compared to the CAD model.

The FEM was simplified by cleaning-up and simplifying the underlying CAD model where possible. For

instance, in the original CAD model, the stringers and the load introduction joints were drawn as separate components and bolted to the skin. In the FEM, these components were merged and attached to the skin using the bonded contact provided by ANSYS Mechanical®. Remaining attachment holes in the skin and stringers were eliminated from the FEM, allowing for a quality quadrilateral mesh.

Members of the actuation mechanism, load introduction joints and stringers are much stiffer than the airfoil skin; hence, they were modelled as rigid. Moreover, the skin thickness is an order of magnitude smaller than the in-plane dimensions. Consequently, it was modelled as a shell. The skin was assigned isotropic material properties. Young's and shear modulus were set to $E = 71$ GPa and $G = 27$ GPa, respectively. A linear material model was used since the strains are expected to remain within the elastic region.

SHELL181 elements were used to model the skin since large deflections are expected to occur during morphing. SHELL181 element is a quadrilateral four-node element with 6 degrees of freedom per node and it is well suited for applications dealing with geometric nonlinearities due to large deflections (ANSYS, 2015a). The rigid morphing mechanism was modelled using the TARGE170 elements connected together with multi-point constraint type of elements, MPC184. MPC184 elements were used to model mechanism hinges as revolute joints with unconstrained rotational degree of freedom about the hinge axis while the remaining degrees of freedom, the three translations and the remaining two rotations were constrained. In order to prevent the rigid body motion of the model, the main spar was connected to the ground using the fixed option of the MPC184 element with all 6 degrees of freedom being fixed. Contacts between the airfoil skin and the lateral stringers were modelled using pairs of CONTA174 and TARGE170 elements which are well suited for general rigid-flexible contact analysis (ANSYS, 2015a). The assembled FEM is shown in Figure 5. The cutout in Figure 5 shows the size of the shell elements used to mesh the airfoil skin. In addition, the finite elements used to model the actuation mechanism are overlaid over the mechanism members.

The mesh of the FEM was checked for convergence using the recommendations by Shah (2002). Shah's recommendation is that the global error norm for the entire FEM, Criterion 1A, is less than 15%, that the local error norm in a high stress area, Criterion 1B, is less than 10%, and that the local stress coefficient of variance in a high stress area, Criterion 1C, is less than 7%. To evaluate the local convergence criteria, the high stress area was chosen between stiffeners 2 and 3 whose location is indicated in Figure 4. The Mesh metric of the FEM and the convergence criteria are summarised in Table 4. According to the listed results, the element size of 3 mm is sufficiently small to obtain a mesh-converged solution.

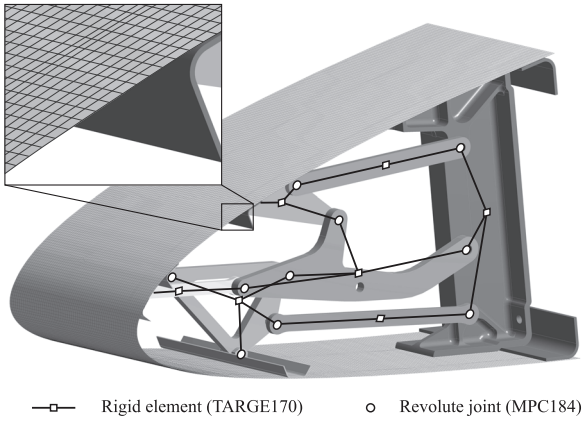

Figure 5. FEM model.

Table 4. FEM summary.

Parameter	Value
Mesh metric	
Element size	3 mm
Number of elements	27,998
Average element aspect ratio	1.09[a]
Maximum element aspect ratio	2.96 ($\leqslant$20)[b]
Mesh convergence[c]	
Criterion 1A	15.2% ($\leqslant$15%)
Criterion 1B	3.6% ($\leqslant$10%)
Criterion 1C	2.8% ($\leqslant$7%)

[a]Optimum aspect ratio: 1 (ANSYS, 2015b).
[b]Recommended maximum aspect ratio: $\leqslant$20 (ANSYS, 2015b).
[c]According to Shah (2002).

4. Results and discussion

Experimental and numerical results obtained during testing are compared and discussed in this section. Shape measurements are presented first, followed by the discussion of the strain results. The morphing mechanism locking test is discussed finally.

4.1. Shape measurements

A preliminary study of the measurement system was performed first to confirm that the demonstrator was actuated consistently and accurately. The study was also used to investigate the consistency and reliability of the photogrammetric method used in the experiment. The leading edge was morphed from zero to a prescribed actuator extension three times. Each time, a picture of the morphed skin was taken and analysed. The results are shown in Figure 6. It can be observed in Figure 6(a) that the edge recognition algorithm was

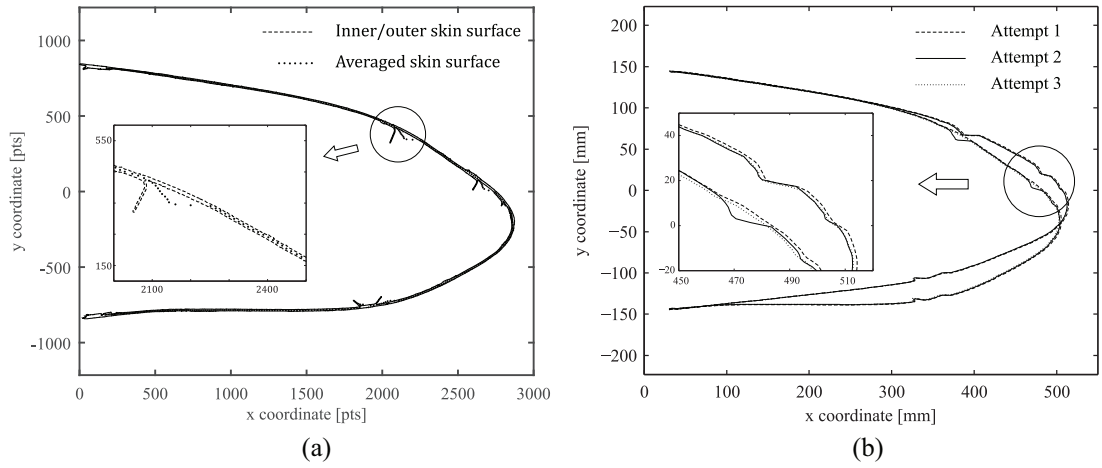

Figure 6. Shape measurement: (a) processed data obtained from the captured pictures of the morphed demonstrator and (b) consistency of the shape acquisition system at different actuator extensions.

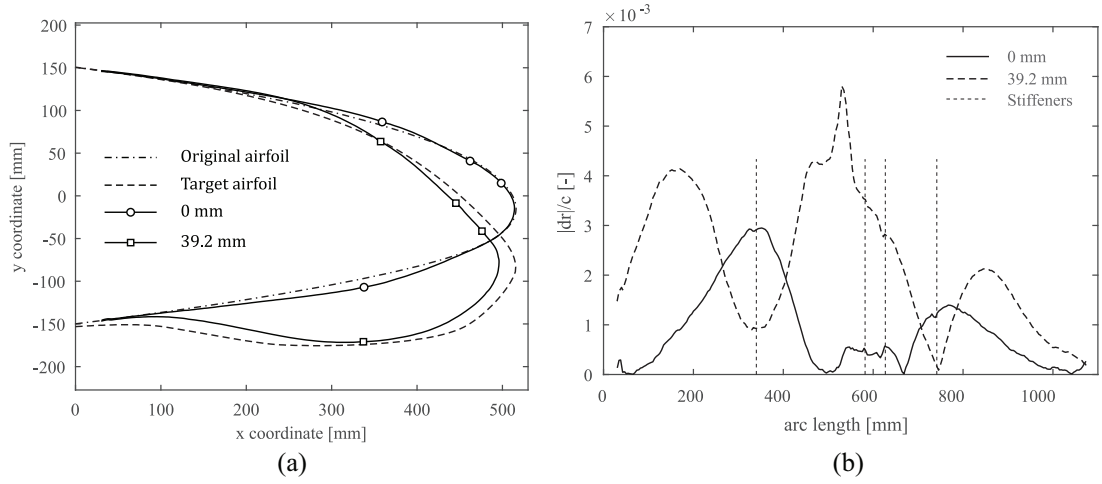

Figure 7. Comparison of the morphed leading edge to the original and target airfoil: (a) experimental results against original and target shape and (b) relative geometric difference.

accurate enough to detect both the outer and inner perimeter of the skin. Consequently, an additional averaging of the acquired measurements was required to obtain the final skin shape. The average shape of the skin is distorted near the lateral stiffeners due to the averaging technique used in the process which also accounted for the points on the stiffeners. The distortions can be observed in the cutout in Figure 6(a). The magnitude of the distortion is greatly dependent on the portion of the lateral stringer that is recognised from the pictures. These distortions represent the only significant source of uncertainty in the edge recognition process, which can be observed in the cutout in Figure 6(b). Consequently, it was decided to physically mask out the lateral stiffeners on the demonstrator before continuing the measurements. The measurement error along the perimeter of the leading edge is calculated as a standard deviation of the measurements at each arc length location. The resulting average measurement error with its standard deviation is 1 mm$\pm$0.6 mm.

In the following step, the demonstrator was compared to the prescribed initial and target shape of the droop nose which were used during the design stage (Figure 5 in Mauchle et al., 2012). The comparison is shown in Figure 7. Geometric comparison of the prescribed original and target airfoil and the morphed demonstrator is shown in Figure 7(a). The chord-normalised minimum Euclidean distance, $|dr|/c$, along the perimeter of the compared leading edge shapes is shown in Figure 7(b). Comparison of the corresponding curvatures is shown in Figure 8.

For a fully retracted actuator, at 0 mm, the demonstrator shape corresponds very well to the prescribed original airfoil everywhere except at the vicinity of the top and bottom stiffener, which is also clearly observable by the two peaks at arc length of 340 and 740 mm

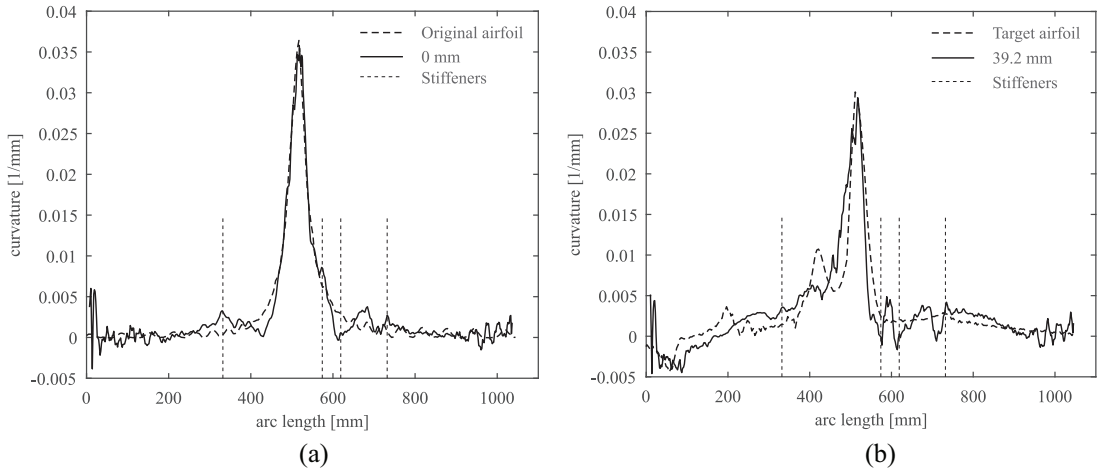

Figure 8. Curvature comparison between the prescribed and measured leading edge shape: (a) actuator extensions of 0 mm and (b) actuator extensions of 39.2 mm.

in Figure 7(b). At the time when the demonstrator was manufactured, the only suitable actuator available in the market was the LINAK LA 23. This actuator was, however, 7 mm too long to allow for the demonstrator to reach its original state even when the actuator is fully contracted.

For a fully extended actuator, at 39.2 mm, the demonstrator follows the contour of the prescribed droop nose very well, especially over the top surface of the airfoil, beyond the arc length of 650 mm. However, there are two notable differences between the morphed demonstrator and the prescribed shape. First, the morphed demonstrator does not maintain the chord length relative to the prescribed target airfoil which leads to the gap of 0.6%c at the tip of the leading edge at arc length of 530 mm. This is a direct consequence of one of the design objectives, namely to avoid stretching of the morphing skin as explained in the 'Introduction' section. The second difference is observed at the bottom section of the skin, up to arc length of 400 mm. The contour of the prescribed target airfoil deviates from the original airfoil much earlier than the morphed demonstrator. Its curvature is also much shallower, almost flat, in the vicinity of the bottom stiffener. The difference is due to the design of the front spar, shown in Figure 1, which protrudes into the leading edge, up to arc length of 100 mm, therewith extending the bottom connection zone between the spar and the skin into the leading edge which limits the morphing skin deformation in that region. Nevertheless, the observed differences are less than 0.4%c.

According to Mauchle et al. (2012), the skin was constrained as clamped at the top and bottom edge, at $x = 0$ in Figure 7(a), during the topology optimisation of the mechanism. The boundary condition was later updated in the detailed design to represent the actual skin-spar connection. However, at this stage, the actuation mechanism was not to change anymore. As seen, the effect of updating the boundary conditions has a significant effect on the achieved morphed shape. Hence, for the future studies, it is worth including the realistic boundary conditions in the design process as early as possible to be able to derive a mechanism which can meet the target shape in the best possible way.

Although the demonstrator was not investigated for aerodynamic performance, the comparison of the curvatures derived from the prescribed original and target leading edge shape and from the measured shapes is shown in Figure 8. Curvature importantly affects the pressure distribution over the wing leading edge region (Thuwis et al., 2010); hence, it is considered an important facet of shape matching. Three remarks can be made about the presented results. First, at the tip of the leading edge at arc length of 520 mm, the curvature of the demonstrator follows the curvature of the prescribed airfoils very well for both actuator extensions of 0.0 and 39.2 mm. Second, oscillations at arc lengths less than 100 mm and more than 900 mm are considered numerical artefacts due to numerical calculation of the second derivative of the leading edge shape with respect to arc length, which is needed for the calculation of the curvature. Numerical differentiation is very sensitive to slight variations in the measured shape if derivatives are close to zero. Finally, one can observe significant deviations of the measured curvatures from the prescribed curvatures in the vicinity of stiffeners on the top surface at arc lengths between 550 and 800 mm. These are attributed to a sudden stiffness change due to the presence of the stiffeners and the fact that the mechanism connection to the skin can only transmit forces and no moments. Such oscillations in the curvature of the leading edge can have detrimental effects on the aerodynamic performance of the proposed morphing concept and should be investigated in more detail.

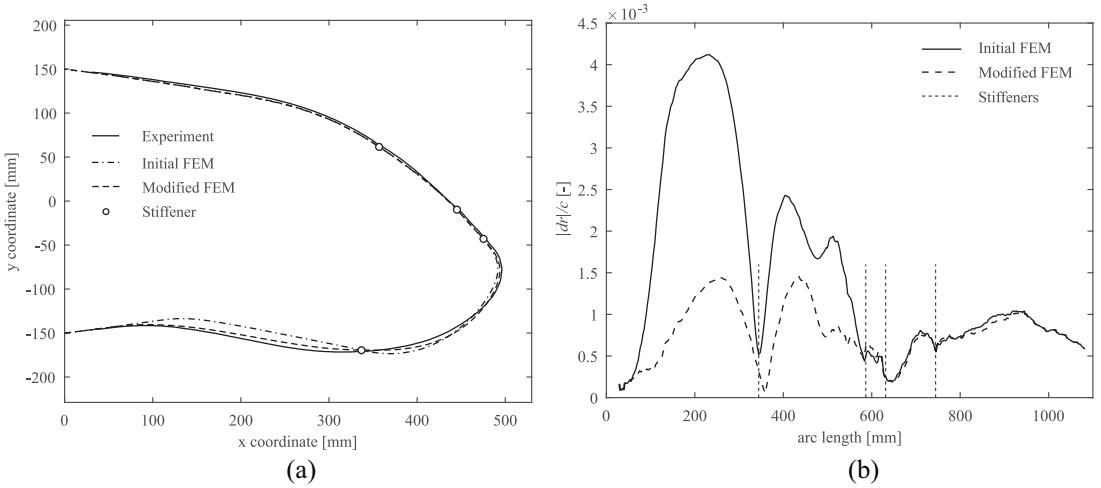

Figure 9. Comparison of the morphed leading edge to FEM at actuator extension of 39.2 mm: (a) experimental results against FEM and (b) relative geometric difference.

In the second part of the shape morphing study, the demonstrator was compared to the FEM. The results for the maximum actuator deflection of 39.2 mm are presented in Figure 9. Figure 9(a) compares the morphed shape of the demonstrator to the initial and modified FEM. The pertinent chord-normalised Euclidean distance between the compared results along the perimeter of the leading edge is shown in Figure 9(b). In general, one can observe good agreement between the demonstrator and both the initial and the modified FEM. The average distance shown in Figure 9(b) is less than 0.15%c and 0.08%c, respectively. The agreement is particularly good at the locations of the lateral stiffeners where the actuation mechanism is attached to the morphing skin. At these locations, assuming a rigid actuation mechanism, the elastic problem of airfoil skin deflection is reduced to a kinematic problem, essentially enforcing the elastic displacement of the skin. As a result, the assumption that the actuation mechanism is essentially rigid relative to the airfoil skin is justified.

The main difference between the initial FEM and the demonstrator is present in the part of the skin up to arc length of 590 mm with the maximum deviation of 0.41%c which originates from the discrepancy between the FEM and the actual demonstrator. During the experiments, the airfoil skin partially peeled off from the bottom skin-spar connection zone allowing the airfoil skin to start deforming much closer to the spar. Interestingly, the effect is noticeable beyond the first stiffener located at the arc length of 340 mm which is attributed to the fact that the stiffeners are free to rotate around the pins connecting them to the actuation mechanism. Consequently, it was decided to modify the initial FEM reducing the size of the bottom skin-spar connection zone to better match that of the demonstrator with the skin partially peeled off.

The agreement between the modified FE model and the demonstrator is significantly improved with the maximum deviation being reduced to just 0.14%c. Despite the modification, the initial and the modified FEM predict almost identical displacements over the top part of the skin, beyond the arc length of 600 mm, which is indicated in Figure 9(b) by nearly identical distance to the morphed demonstrator shown along this part of the skin.

During every morphing action, the actuator extension and the actuation force were monitored. Four different extensions and their respective actuation forces over time are shown in Figure 10(a) and (b), respectively. According to the measurements, there is an initial force build-up period, up to 1 s, at the beginning of every morphing action. During this period the actuation force is rapidly rising while the actuator is still not moving. The actuator must first reach the break-away force to overcome the static friction in the actuation mechanism. Once the mechanism starts moving, a sharp drop in the actuation force, ΔF_{act}, can be observed, which is attributed mainly to the difference between the static and kinetic friction in the mechanical joints. It is interesting to note that the required actuation force keeps decreasing until an actuation extension of approximately 20 mm is reached. Then, the actuation force starts increasing again.

The continuous decrease in the required actuation force is attributed to the kinematic properties of the morphing mechanism. While the actuator is being extended, the morphing loads are increasing. However, the leverage between individual mechanism members is also changing due to their relative rotations. Initially, the change in the mechanism leverage alleviates the loads on the actuator faster than the morphing loads increase.

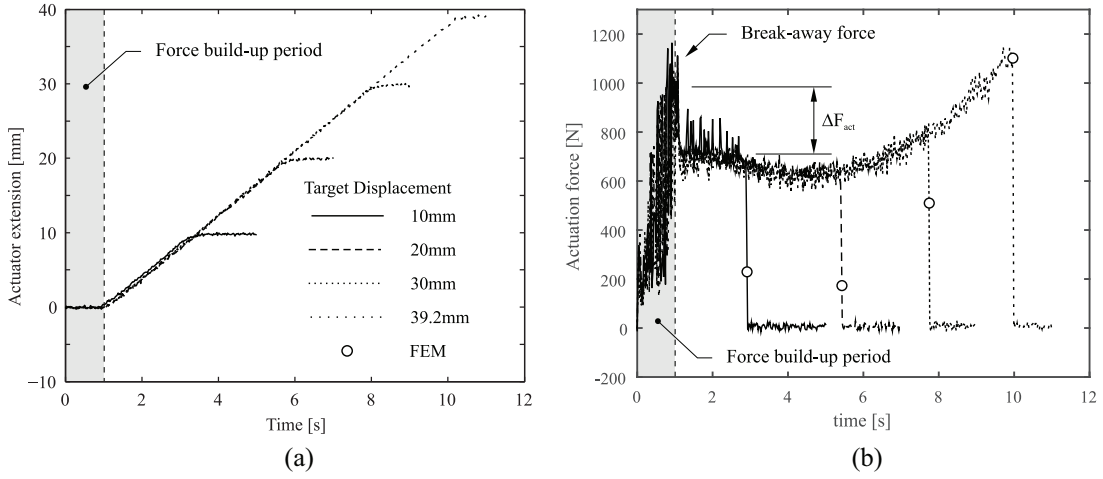

Figure 10. Actuation in time: (a) actuator extension and (b) actuation force.

Actuation force is also compared to the FEM results. Even though the material properties of the airfoil skin in the FEM simulations were selected to resemble aluminium, the overall agreement is not good. For most of the actuator extension, the FEM forces significantly underpredict the measured actuation force, which can be attributed, first, to the fact that friction in the mechanism joints was not taken into account in the FEM, and second, the actuation force was measured indirectly by measuring the current drawn by the actuator, which also includes all the internal losses in the actuator itself. However, at actuator extension of 39.2 mm, the FEM actuation force is almost equal to the measured actuation force.

Both the actuator extension and the actuation force were also analysed for the measurement error. The measured actuator extension was compared to the requested actuator extension. The average error with its standard deviation of 0.13mm±0.09mm was found across all the measurements. The measurement error is at an order of 1% of a typical actuator extension considered in this study.

The assessment of the measurement error in the case of the actuation force was split in two parts. Over the force build-up period, up to $t = 1$ s, while the actuator is not moving, the measurement error was estimated to be on average 182 N±73 N. The found measurement error is relatively high at an order of 20% of the maximum actuation force over this period. In the second part, over the period, when the actuator is moving, for $t>1$ s, the average measurement error with its standard deviation was considerably lower, 30 N±17 N, which is at an order of 2%–5% over the range of measured actuation forces. The difference is assumed to be due to the fact that during the force build-up phase, the actuator must overcome the transient electrical loads as well as the static friction in all the mechanical components of the actuator and the morphing mechanism which leads to a very noisy behaviour of the measured force. Nevertheless, an exact cause of these large fluctuations remains to be determined.

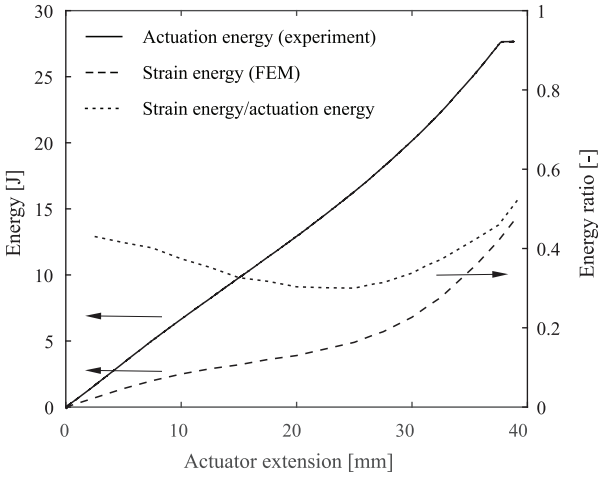

Figure 11. Actuation energy.

Next, the actuation force is integrated with respect to the actuator extension in order to obtain the overall actuation energy required to execute a morphing action. The actuation energy as a function of actuator extension is compared to the strain energy of the morphing skin obtained by the FE analysis in Figure 11. The strain-to-actuation-energy ratio indicates that, on average, only 35% of the actuation energy is used for morphing the airfoil skin, while the rest is lost in the actuation mechanism.

There are two further comments required regarding the actuation and strain energy shown in Figure 11. First, the actuation force over the force build-up period does not contribute to the calculated actuation energy since the actuator displacement remains zero. In reality, some electric energy is spent on powering the actuator

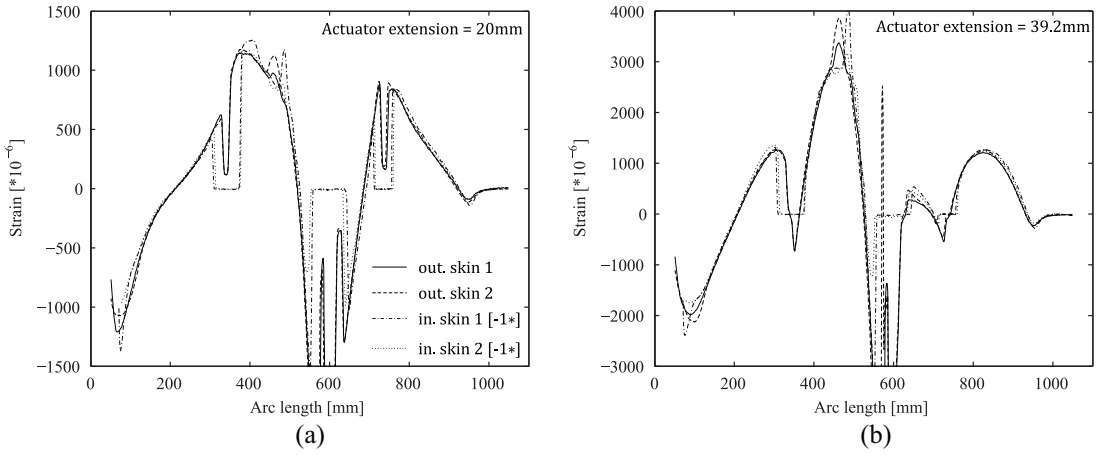

Figure 12. Symmetry analysis: (a) actuator extension of 20 mm and (b) actuator extension of 39.2 mm.

to overcome the initial static friction of the mechanism. Hence, the overall energy spent on morphing will be higher than the predicted actuation energy. Second, the strain energy of the morphing skin was reduced by 1.1 J to account for the initial deformation of the morphing skin due to the actuator size as explained in the preceding section on shape measurements. The resulting strain energy therefore corresponds to the strain energy due to the actuator extension only.

4.2. Strain

Geometrical analysis of the morphing leading edge demonstrator showed good agreement with both prescribed original and target shape as well as with the FEM. Another critical aspect to investigate is how and to what extent is the airfoil skin deformed during the morphing process by analysing the induced strains. For the sake of clarity, only the results pertinent to the modified FEM are shown.

The consistency of the measured strains is investigated first by comparing the measurements on the inner and outer surface of the airfoil skin at two spanwise locations and by assessing the measurement error. The results for two different actuator extensions, 20 mm and 39.2, are shown in Figure 12. The strain is given as a function of arc length along the airfoil skin starting at the bottom of the airfoil next to the main spar. As mentioned, strains were measured at two spanwise locations. The corresponding results are hence labelled 1 and 2. Moreover, strains measured on the outer and inner surface of the airfoil skin are labelled out. skin and in. skin, respectively. The strain measured on the inner surface is multiplied with a factor of –1 to ease the comparison with the measurements on the outer surface of the airfoil skin. A factor of –1 is selected since the respective strains are expected to be of the opposite sign due to the premise of the actuation mechanism design that morphing should be mostly driven by bending deformation of the airfoil skin. Finally, one can observe that zero strains were measured on the inner surface along some sections of the leading edge perimeter. These measurements coincide with the locations where the fibre optic sensor is not attached to the structure as it has to traverse the lateral stiffeners.

The comparison of the measured strains pertinent to locations 1 and 2 shows that the strains match remarkably well for both outer and inner surface of the skin and both actuation extensions. The measured strains are almost identical in this regard. This leads to a conclusion that the morphing mechanism is rigid enough to provide exact and uniform skin deformation across the entire width of the leading edge without any unwanted skewing or twisting. Moreover, the magnitude of the strain on the inner surface of the airfoil skin represents an almost perfect reflection of the strains measured on the outer surface, which suggests that the induced morphing is indeed predominantly driven by bending.

At the maximum actuator extension of 39.2 mm, three strain measurements were acquired. The measurement error along the fibre optic was then estimated as the standard deviation of the measured strains across the three measurement sets. The average error with its standard deviation was found to be 10 micro-strains $\pm$ 113 micro-strains. The high standard deviation of the estimated measurement error is mainly due to the high measurement error in the regions of high strain rates, between arc lengths of 550 and 620 mm. However, if the maximum 1% of the measurement errors is omitted from the error analysis, the pertinent standard deviation drops to $\pm$1 micro-strain.

Strain data obtained by the fibre optic sensor on the outer surface of the airfoil are compared with the results from the FEM. Raw strains at two different actuator displacements are shown in Figure 13. The measured and the numeric strains are, in general, in good agreement except near the stiffeners and close to the bottom connection to the main spar, at the arc

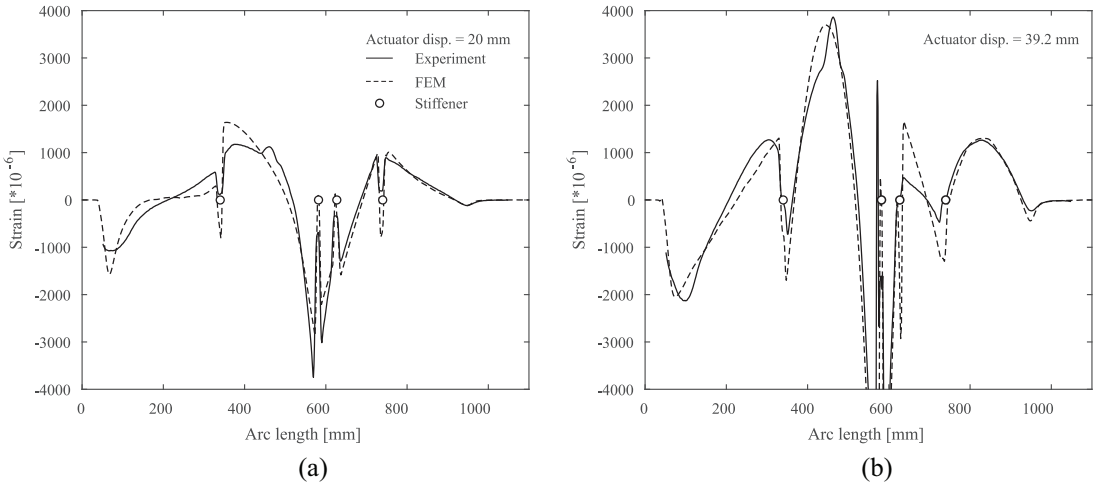

Figure 13. Comparison of measured and FEM strains: (a) actuator extension of 20 mm and (b) actuator extension of 39.2 mm.

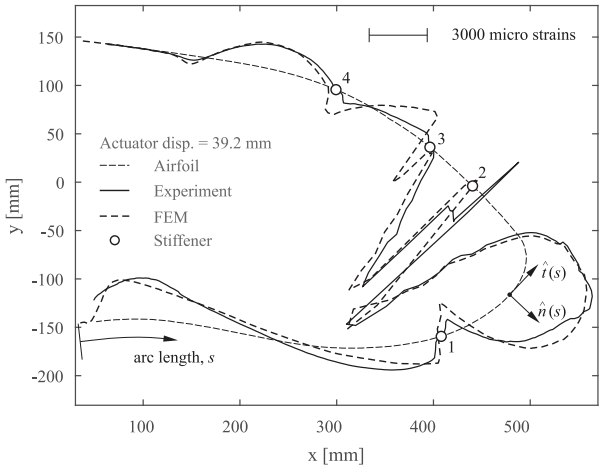

Figure 14. Measured and FEM strains mapped to the morphed airfoil skin.

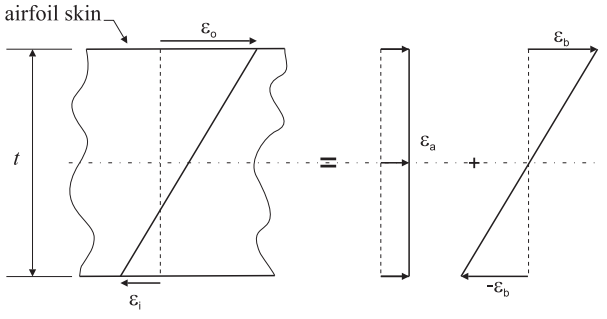

Figure 15. Strain decomposition.

length of 50 mm. In these areas, the numeric results predict higher strain values. Strain is also concentrated closer to the stiffeners. Such behaviour is attributed to the stiffeners being modelled as rigid, forcing the skin to strain more. Otherwise, good agreement was expected since the measured and the calculated morphed geometries of the leading edge presented in Figure 9(b) also show good overall agreement.

Strains corresponding to the actuator extension of 39.2 mm are also mapped to the morphed airfoil in Figure 14 highlighting regions of high deformations. Strain values along the outward normal of the airfoil contour are considered positive. It shows that the highest strains, both positive, tensile strains as well as negative, compressive strains, are encountered at the very tip of the leading edge between the first and the second stiffener. High compressive strains are also encountered between the second and the third stiffener. It is noteworthy that Figures 13 and 14 present only the strains on the outer surface, meaning that the nature of the underlying deformation of the airfoil skin, such as stretching or bending, cannot be deduced based on these data only.

Further analysis of the available strain data was performed to obtain better insight into the amount of bending and axial strain present in the induced deformation. Typical strain behaviour in the airfoil skin during morphing is shown in Figure 15. Since the skin was relatively thin and there were only two strain measurements available through the skin thickness, namely, on the inner and outer surface of the skin, a linear through-thickness behaviour of the strains was assumed. Consequently, axial strain, ε_a, was calculated as an average of the strains on the outer and inner skin, ε_o and ε_i, respectively: $\varepsilon_a = (\varepsilon_o + \varepsilon_i)/2$. While bending strain, ε_b, was calculated as: $\varepsilon_b = (\varepsilon_o - \varepsilon_i)/2$. The results for bending and axial strains at two different actuator displacements are depicted in Figures 16 and 17. Again, in regions where the optic fibre sensor could not be attached to the skin surface, the data are missing. Consequently, the measured strains are not continuous around the entire perimeter of the leading edge.

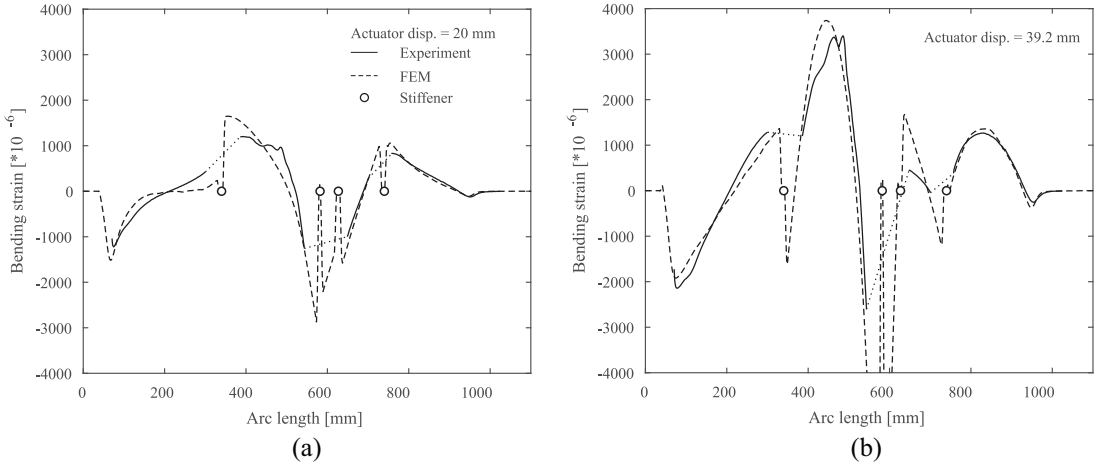

Figure 16. Comparison of bending strains: (a) actuator extension of 20 mm and (b) actuator extension of 39.2 mm.

Experimental and numeric bending strains exhibit very good agreement, except in the very vicinity of the stiffeners, where the FEM tends to over-predict the experimental results. According to the FEM, the bending deformation is more localised near the stiffeners, which is reflected by narrower and sharper peaks in the FEM strain plots.

Agreement in the axial strains is worse. The numeric strains are close to zero showing little variation along the perimeter of the airfoil skin, except at the stiffener locations, where the numerical strains show sharp peaks which are explained by sudden stiffness change due to rigid stiffeners. As a result, there is no strain induced on the inner surface where the skin attaches to the stiffeners. Therefore, following the procedure outlined in Figure 15 leads to high axial strains which equal to half of the strain obtained on the outer surface of the airfoil skin. Experimental strains show more variation along the perimeter of the leading edge especially for the higher actuator displacement of 39.2 mm. Relatively high compressive strains are observed at the arc length of about 500 mm, between the first and the second stiffener. In combination with the stiffness and geometrical properties of the skin panels in such regions, high compressive strains might indicate a buckling critical area which would have to be accounted for in the design process. Nevertheless, no buckling was detected during the current set of experiments. Finally, one can observe some oscillations in the experimental strain, such as those at arc lengths of 88 and 476 mm. These oscillations appear in the areas of very high strain rates as can be observed in Figure 12. Hence, a slight misalignment of the measurement points along the arc length between the outer and the inner surface can lead to a significant error in the acquired axial strain. These oscillations are therefore largely attributed to the misalignment error in positioning the inner and outer strains with respect to each other.

Comparing the magnitude of the axial and bending strains, the axial strains appear to be an order of magnitude smaller than the corresponding bending strains which confirms one of the main design premises that drooping of the leading edge should be driven predominantly by bending deformation in order to be able to achieve large deformations while keeping the actuation forces as low as possible.

It is important to point out that no aerodynamic or equivalent distributed loads were applied on the airfoil skin in the current experiments. Therefore, it remains to be investigated what the effect of these loads in combination with morphing deflection on the overall strain values induced in the morphing skin is.

Although fatigue life assessment of the presented demonstrator is beyond the scope of this article, given the strain levels observed at a maximum actuator displacement of 39.2 mm, a remark about possible fatigue issues is necessary. For reference, the 7075T6 aluminium comprising the airfoil skin yields at 8860 micro-strain (U.S. Department of Defense, 1998). The maximum axial strain of 681 micro-strains represents less than 10% of the yield strain. It is therefore not a concern. On the other hand, the maximum bending strain of 3403 micro-strains is of comparable magnitude as the yield strain. Even though the flexural fatigue is less severe than axial fatigue due to the lesser volume fraction of the material being exposed to high strain/stress levels, the airfoil skin could be susceptible to low-cycle fatigue (Manson and Muralidharan, 1987). However, in the current case, the airfoil skin was manufactured from a constant thickness isotropic material. Therefore, the high bending strains could be resolved, if necessary, by allowing for a variable thickness and stiffness tailoring of the morphing skin along the perimeter of the leading edge.

4.3. Locking of the morphing mechanism

Experimental results in terms of the nodal displacement and skin strain due to external load are presented in

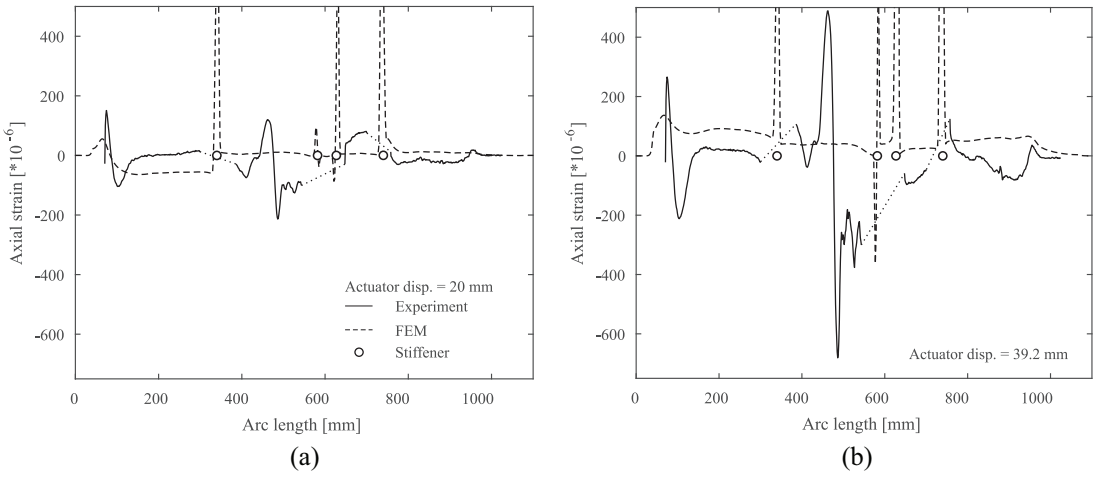

Figure 17. Comparison of axial strains: (a) actuator extension of 20 mm and (b) actuator extension of 39.2 mm.

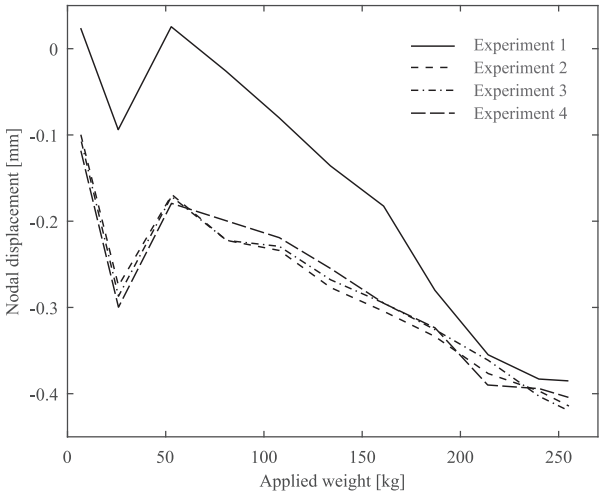

Figure 18. Deformation of the morphing mechanism.

this section to evaluate the locking of the morphing mechanism. During this experiment, a total load of 2500 N was gradually applied via a system of pulleys and weights as shown in Figure 3. The experiment was repeated four times to be able to assess the consistency of the mechanism behaviour.

The displacement of the selected node is presented in Figure 18. The results show two interesting features. First, at the maximum load, the mechanism undergoes a maximum displacement of 0.4 mm. Second, the displacement measurements are very consistent over the performed set of experiments except for Experiment 1. Experiment 1 deviates from the others, which is attributed to the presence of some initial free-play in the mechanism before applying the load for the first time. The measurement error as a function of applied load was estimated as standard deviation of the measured nodal displacement across the Experiments 2, 3 and 4. Experiment 1 was excluded from the error analysis due to being an outlier. The average error with its standard deviation was found to be 0.01 mm$\pm$0.004 mm.

From the collected data it is not possible to discern whether the 0.4 mm displacement is due to the mechanism deformation or due to the remaining free-play in the joints of the mechanism. Such mechanism displacements can have a detrimental effect on the ability of the mechanism to maintain an accurate aerodynamic shape of the leading edge over the range of operating conditions. In addition, changing values of mechanism free-play can also lead to higher actuation forces due to the increased friction. The effect of mechanism stiffness and production tolerances therefore remains an important aspect to include in the future design studies.

During the application of the load, strains were also measured using strain gauges at the selected locations on the morphing skin as shown in Figure 4. The measured axial and bending strains are depicted in Figure 19(a) and (b), respectively. Strain gauge 2 and 8 were damaged during the experiment, hence their values are not shown. For the remaining strain gauges, it can be observed that the maximum magnitude of the bending and axial strain at the maximum applied load reaches roughly 2000 and 350 micro-strain, respectively. Both peaks are reached at the location of strain gauge 4, which is located near the most forward load introduction point, where also most of the consolidated aerodynamic load was applied. Moreover, the bending strain measured by strain gauge 1, close to the top skin-spar connection, is only 100 micro-strain which is an order of magnitude less than the maximum bending strain observed by the strain gauge 4. Based on the obtained results, one can conclude that most of the applied load was taken by the morphing mechanism while the airfoil skin remained relatively unstrained. This demonstrates the capability of the mechanism to provide

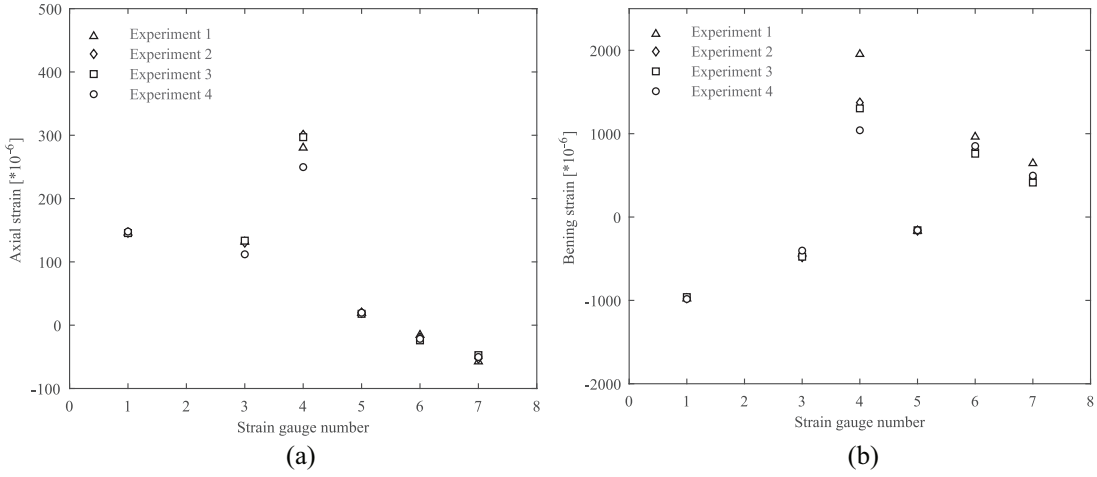

Figure 19. Measured strains at applied consolidated load of 255.2 kg: (a) axial strain and (b) bending strain.

structural support to the morphing skin. As a result, such mechanism design would allow for a more compliant morphing skin and would prevent the formation of stress/strain concentrations in the vicinity of the skin-spar connections due to external loads.

Finally, the measurement errors for both axial and bending strains were evaluated similar to the nodal displacement of the mechanism. The average errors in axial and bending strain were found to be 8 micro-strains ± 11 micro-strains and 54 micro-strains ± 62 micro-strains, respectively.

4.4. Discussion and future work

The performed experimental investigation improves the understanding of the structural and morphing performance of the tested morphing leading edge demonstrator and to a certain extent validates the design process employed to design the demonstrator. Nevertheless, a number of important issues with the current demonstrator itself as well as with the design process in general have been identified which still have to be addressed in order to be able to improve the design of such morphing devices and increase their maturity.

One of the most important aspects that remains to be investigated is aerodynamic performance of the designed morphing leading edge. Such an investigation should comprise an aeroelastic analysis, either numeric or experimental, of the leading edge shape in its cruise as well as high-lift configurations in order to provide at least three insights. First, how does the morphing skin deformation under the aerodynamic loads affect the aerodynamic performance of the leading edge in both cruise and high-lift configurations. Second, how do the aerodynamic loads influence the overall strain levels in the airfoil skin during morphing. Third, a quality metrics for the achieved morphed shape such that one can gauge the quality of the actuation mechanism design in a more objective way.

From structural and morphing standpoint, an important concept for future investigations is stiffness and thickness tailoring of the morphing skin. As shown by Thuwis et al. (2010), tailoring can be used for better matching the prescribed target shape as well as for mitigating the high strain levels due to morphing. Both aspects, however, remain to be validated.

Moreover, the comparison of the curvatures between the measured and target airfoil shape revealed that the stiffeners significantly distort the curvature of the morphing skin in their vicinity which could be critical from aerodynamic point of view. Therefore, it is important to investigate whether it is possible to achieve a more blended skin-stiffener connection using skin tailoring in order to suppress this kind of curvature distortions.

In terms of actuation mechanism design, several aspects such as free-play, friction and scalability remain to be investigated. In this study, some free-play was detected in the mechanism joints. It is not yet clear, first, what is the effect of such free-play on the accuracy of the leading edge shape in both cruise and high-lift configurations, and second, what amount of free-play is still acceptable. Moreover, the effect of free-play in combination with friction on the required actuation force once the leading edge is subjected to aerodynamic loads must be also investigated. Finally, the demonstrator was built as a two-dimensional (2D) section of a wing. Hence, it remains to perform a scale-up study to investigate aspects such as the required pitch of the actuation mechanism along the wing span and three-dimensional (3D) effects such as skin warping when deformed.

Finally, to be able to advance the technology readiness level of such a concept, one needs to consider also operational and certification requirements. A fatigue and life cycle analysis is required in order to ensure sufficient longevity of the morphing skin and actuation

mechanism. In addition to stress/strain effects, such an assessment should also address effects related to material ageing and abrasion due to exposure to environment. In terms of certification requirements, bird-strike and de-icing, among others, have to be considered. These issues have been already addressed to a certain extent within the SARISTU project (Wölcken and Papadopoulos, 2016). Nevertheless, it remains to be investigated whether any of the proposed solutions can be adapted to the currently investigated concept.

5. Conclusion

Experimental evaluation of the morphing leading edge concept is presented in this article. In addition, the experimental results are compared to the FE results. The experimental trials were designed to test the morphing demonstrator with respect to the most important requirements imposed during the design stage of the LeaTop project. The primary design requirements were as follows: (1) capability of matching the prescribed target airfoil, (2) ensure that morphing is dominated by bending deformation and (3) ensure that the transfer of aerodynamic loads from the skin to the main spar is achieved via the morphing mechanism. The acquired results show that the morphing leading edge demonstrator successfully meets all of the design requirements.

Airfoil shape measurements reveal a good match with the prescribed target shape of the demonstrator as well as with the morphed shape obtained using the FEM. The only significant difference with respect to the prescribed target shape was detected near the bottom skin-spar connection due to the spar design protruding in the leading edge. A noticeable difference between the experiment and the initial FEM was observed in this area as well which was attributed to the airfoil skin peeling off from the skin-spar connection. However, once the FEM was updated to account for this effect, the match between the experiments and the FE results was very good along the entire perimeter of the leading edge for all actuator displacements.

Strain measurements show that morphing is dominated by bending the airfoil skin rather than stretching it. The axial strains are at least an order of magnitude smaller than the bending strains over most of the airfoil skin. Moreover, comparison with the FE results shows very good agreement in general for both bending and axial strains at all levels of actuator displacements. Substantial differences are only observed close to mechanism attachment points which are attributed to the stiffeners being modelled as rigid allowing for zero strain on the contact surface.

The measured actuation force shows that a significant break-away force is required to overcome static friction in the actuation mechanism. Comparison of the measurements to the numerical results reveals that the actuation forces significantly disagree even though the morphed shape of the leading edge and the corresponding strains agree very well. There are two main reasons for the observed differences between the numeric and experimental actuation force. First, the actuation force was measured indirectly by measuring electric power consumed by the actuator which in addition to morphing loads and friction forces accounts also for all the electrical losses in the actuator. Second, the FEM did not account for friction in the actuation mechanism.

Finally, in the case of the morphing mechanism locking capabilities, the results show that the mechanism is effectively locked under consolidated aerodynamic loads such that only minimum displacement in the measured mechanism node is observed. Strain measurements show that the mechanism can support the skin by absorbing and transferring most of the applied load to the main spar as indicated by the low strain values. Consequently, a more compliant morphing skin can be employed and the stress/strain concentrations close to the skin-spar connections can be reduced.

Acknowledgements

The authors would like to acknowledge Alexander R. Mauchle for the design and Arne Slingerland for the assembly of the presented morphing leading edge demonstrator.

Declaration of conflicting interests

The author(s) declared no potential conflicts of interest with respect to the research, authorship and/or publication of this article.

Funding

The author(s) disclosed receipt of the following financial support for the research, authorship, and/or publication of this article: The work presented herein has been partially funded by the European Community's CleanSky Green Regional Aircraft programme under the Grant Agreement 271861. The LeaTop project (Leading Edge Actuation Topology Design and Demonstration) is a CfP project funded under the topic SP1-JTI-CS-2010-03. The project started on February 1st 2011 and was concluded successfully on February 28th 2013.

ORCID iDs

Jurij Sodja https://orcid.org/0000-0001-8347-1438
Marcias J Martinez https://orcid.org/0000-0002-3985-9926

References

ACARE (2010) 2008 Addendum to the strategic research agenda. Available at: www.acare4europe.org
ANSYS (2015a) *Mechanical APDL* Element Reference, Release 15.0. Cheyenne, WY: SAS IP, Inc.
ANSYS (2015b) Mechanical APDL Theory Reference, Release 15.0. Cheyenne, WY: SAS IP, Inc.

Barbarino S, Bilgen O, Ajaj RM, et al. (2011) A review of morphing aircraft. *Journal of Intelligent Material Systems and Structures* 22(9): 823–877.

Casalino D, Diozzi F, Sannino R, et al. (2008) Aircraft noise reduction technologies: a bibliographic review. *Aerospace Science and Technology* 12(1): 1–17.

De Gaspari A and Ricci S (2011) A two-level approach for the optimal design of morphing wings based on compliant structures. *Journal of Intelligent Material Systems and Structures* 22(10): 1091–1111.

De Gaspari A and Ricci S (2014) Application of the active camber morphing concept based on compliant structures to a regional aircraft. In: Farinholt KM and Griffin SF (eds) *Proceedings of SPIE*, vol. 9059, San Diego, Calif, USA, April 2014, pp. 1–21. Bellingham, WA: The International Society for Optical Engineering.

De Gaspari A, Ricci S and Riccobene L (2016) Design, manufacturing and wind tunnel test of a morphing wing based on compliant structures. In: *24th AIAA/AHS adaptive structures conference*, San Diego, CA, 4–8 January, pp. 1–18. Reston, VA: American Institute of Aeronautics and Astronautics.

Dobrzynski W, Gehlhar B and Buchholz H (2001) Model and full scale high-lift wing wind tunnel experiments dedicated to airframe noise reduction. *Aerospace Science and Technology* 5(1): 27–33.

Graham W, Hall C and Vera Morales M (2014) The potential of future aircraft technology for noise and pollutant emissions reduction. *Transport Policy* 34: 36–51.

Güemes A, Fernández-López A and Soller B (2010) Optical fiber distributed sensing – physical principles and applications. *Structural Health Monitoring: An International Journal* 9(3): 233–245.

Kintscher M, Geier S, Monner HP, et al. (2014) Investigation of multi-material laminates for smart droop nose devices. In: *29th congress of the International Council of the Aeronautical Sciences (ICAS 2014)*, St. Petersburg, 7–12 September, pp. 1–11. Bonn: ICAS.

Kintscher M, Wiedemann M, Monner HP, et al. (2011) Design of a smart leading edge device for low speed wind tunnel tests in the European project SADE. *International Journal of Structural Integrity* 2(4): 383–405.

Kirn J and Storm S (2014) Kinematic solution for a highly adaptive droop nose. In: *Proceedings of ICAST*, pp. 1–11. Available at: http://library.eawag-empa.ch/icast_proceedings_2014_open_access/ICAST2014015.pdf

Linak (2012) LA23: compact and strong electric push and pull actuator. Available at: https://www.linak.com/

Luna Innovations Inc (2012) LUNA optical distributed sensor interrogator. Available at: http://lunainc.com/

Manson SS and Muralidharan U (1987) Fatigue life prediction in bending from axial fatigue information. *Fatigue & Fracture of Engineering Materials & Structures* 9(5): 357–372.

Mauchle AR, De Breuker R, Thuwis GAA, et al. (2012) Design and demonstration of a leading edge actuation system, through topology optimisation. In: *23rd international conference on adaptive structures and technologies (ICAST 2012)*, Nanjing, China, 11–13 October, pp. 418–429. Nanjing, China: Nanjing University of Aeronautics and Astronautics.

Monner H, Kintscher M, Lorkowski T, et al. (2009) Design of a smart droop nose as leading edge high lift system for transportation aircrafts. In. *50th AIAA/ASME/ASCE/AHS/ASC structures, structural dynamics, and materials conference*, Palm Springs, CA, 4–7 May, pp. 1–10. Reston, VA: American Institute of Aeronautics and Astronautics.

Monner H, Riemenschneider J and Kintscher M (2012) Groundtest of a composite smart droop nose. In: *53rd AIAA/ASME/ASCE/AHS/ASC structures, structural dynamics and materials conference*, Honolulu, HI, 23–26 April. Reston, VA: American Institute of Aeronautics and Astronautics.

Morgan HL (1986) High-lift flaps for natural laminar flow airfoils. In: Laminar *f*low *a*ircraft *c*ertification, Wichita, KS, 15–16 April 1985, pp. 31–65. Hampton, VA: NASA Langley Research Center.

Rudenko A, Hannig A, Monner HP, et al. (2018) Extremely deformable morphing leading edge: optimization, design and structural testing. *Journal of Intelligent Material Systems and Structures* 29(5): 764–773.

Shah C (2002) Mesh discretization error and criteria for accuracy of finite element solutions. In: *Ansys users conference*, pp. 1–12. Available at: https://www.ansys.com/-/media/ansys/corporate/resourcelibrary/conference-paper/2002-int-ansys-conf-9.pdf

Suder K (2012) Overview of the NASA environmentally responsible aviation project's propulsion technology portfolio. In: *48th AIAA/ASME/SAE/ASEE joint propulsion conference & exhibit*, Atlanta, GA, 30 July–1 August. Reston, VA: American Institute of Aeronautics and Astronautics.

Thuwis GAA, Abdalla MM and Gürdal Z (2010) Optimization of a variable-stiffness skin for morphing high-lift devices. *Smart Materials and Structures* 19(12): 124010.

Thuwis GAA, De Breuker R and Simpson J (2011) Conceptual design of an actuation system for a morphing leading edge high-lift device using topology. In: *22nd International conference on adaptive structures and technologies (ICAST 2011)*, Corfu, 10–12 October.

U.S. Department of Defense (1998) *Metallic Materials and Elements for Aerospace Vehicle Structures*. Washington, DC: U.S. Department of Defense.

Vasista S, De Gaspari A, Ricci S, et al. (2016) Compliant structures-based wing and wingtip morphing devices. *Aircraft Engineering and Aerospace Technology* 88(2): 311–330.

Vasista S, Riemenschneider J and Monner HP (2015) Design and testing of a compliant mechanism-based demonstrator for a droop-nose morphing device. In: *23rd AIAA/AHS adaptive structures conference*, Kissimmee, FL, 5–9 January, pp. 1–15. Reston, VA: American Institute of Aeronautics and Astronautics.

Weisshaar TA (2013) Morphing aircraft systems: historical perspectives and future challenges. *Journal of Aircraft* 50(2): 337–353.

Wölcken PC and Papadopoulos M (2016) *Smart Intelligent Aircraft Structures (SARISTU): Proceedings of the Final Project Conference*. Cham: Springer International Publishing.